

ANALYSIS OF BEAM HARDENING STREAKS IN TOMOGRAPHY

ALEXANDER KATSEVICH

ABSTRACT. The mathematical foundation of X-ray CT is based on the assumption that by measuring the attenuation of X-rays passing through an object, one can recover the integrals of the attenuation coefficient $\mu(x)$ along a sufficiently rich family of lines L , $\int_L \mu(x)dx$. This assumption is inaccurate because the energy spectrum of an X-ray beam in a typical CT scanner is wide. At the same time, the X-ray attenuation coefficient of most materials is energy-dependent, and this dependence varies among materials. Thus, reconstruction from X-ray CT data is a nonlinear problem. If the nonlinear nature of CT data is ignored and a conventional linear reconstruction formula is used, which is frequently the case, the resulting image contains beam-hardening artifacts such as streaks. In this work, we describe the nonlinearity of CT data using the conventional model accepted by all CT practitioners. Our main result is the characterization of streak artifacts caused by nonlinearity. We also obtain an explicit expression for the leading singular behavior of the artifacts. Finally, a numerical experiment is conducted to validate the theoretical results.

1. INTRODUCTION

X-ray Computer Tomography (CT) is a ubiquitous imaging tool used in numerous applications, including medical imaging, nondestructive testing, industrial metrology, and security scanning. Let $\mu(x)$ denote the X-ray attenuation coefficient at point x inside an object. The mathematical foundation of CT is based on the assumption that by measuring the attenuation of X-rays passing through the object, one can recover the integrals of $\mu(x)$ along a sufficiently rich family of lines L , $\int_L \mu(x)dx$.

This assumption is usually inaccurate because the vast majority of conventional X-ray sources generate X-ray beams with a wide spectrum supported on an interval $[0, E_{\text{mx}}]$ [24, section 4.2], [10]. Here E_{mx} is the maximum energy of photons in the beam. At the same time, the X-ray attenuation coefficient of the vast majority of materials depends on energy, and this dependence differs for different materials. Hence, it is more appropriate to describe the attenuation coefficient as a function of position x and energy E , that is, $\mu(x, E)$. Thus, using Beer's law, the CT data, $g(L)$, can be written in the form

$$(1.1) \quad g(L) = -\ln \left[\int_0^{E_{\text{mx}}} \rho(E) \exp \left(- \int_L \mu(x, E) dx \right) dE \right].$$

Here $\rho(E)$ denotes the intensity of the beam at energy E multiplied by the efficiency of the X-ray detector at energy E . In practice, CT data are normalized (by performing the so-called offset and gain correction), so we

assume $\int_0^{E_{\max}} \rho(E) dE = 1$. If $\rho(E) \approx \delta(E - E_0)$ for some E_0 , then (1.1) does provide line integral data for the function $\mu(x, E_0)$:

$$(1.2) \quad g(L) = \int_L \mu(x, E_0) dx.$$

In most cases, the spectrum $\rho(E)$ is spread out; therefore, the assumption $\rho(E) \approx \delta(E - E_0)$ is not accurate.

Ignoring the dependence of μ on E during reconstruction leads to the appearance of beam-hardening artifacts (BHA). There are three types of BHA: cupping (see Figure 10), dark localized strips between objects with an effective atomic number higher than the background, and streaks (see Figure 11 for the last two artifacts).

For some objects, it is possible to remove the BHA using CT data preprocessing [15], [29, p. 795] and [9, Section 12.5]. Suppose $\mu(x, E) = \mu(E)f(x)$. Here, μ is a *known* function that depends only on energy, and $f(x)$ is an *unknown* function that depends only on position and needs to be reconstructed. This approximation is fairly accurate, for example, for biological soft tissues, because they consist primarily of water. Therefore, when imaging anatomical regions with minimal amounts of bone, we obtain $\mu(E) = \mu_w(E)$. The latter is the well-known attenuation coefficient of water as a function of energy. Consequently, the function $f(x)$ is the water-calibrated density of the tissue at point x .

Assuming the above model, we can rewrite (1.1) as

$$(1.3) \quad \begin{aligned} g(L) &= G(t), \quad G(t) = -\ln \left[\int_0^{E_{\max}} \rho(E) \exp(-\mu(E)t) dE \right], \\ t &= (Rf)(L) = \int_L f(x) dx, \end{aligned}$$

where R denotes the classical two-dimensional (2D) Radon transform. The function G increases monotonically and its inverse, G^{-1} , can be easily obtained. Subsequently, $G^{-1}(g(L))$ provides accurate line integral data for f . When $\mu = \mu_w$, this procedure is called soft tissue correction [15] or water pre-correction [29, p. 795].

However, most of the time, the assumption $\mu(x, E) = \mu(E)f(x)$ is not accurate. For example, bones and soft tissues/water have very different dependencies of the attenuation coefficient on energy in the interval $[0, E_{\max}]$ [15, Fig. 1], [16, 31]. Similarly, metals (such as pacemakers and hip implants), which may appear inside the human body, exhibit a very different dependence of the attenuation coefficient on energy from water and bone.

As a more accurate approximation, one can suppose that

$$(1.4) \quad \mu(x, E) = \mu_1(E)f_1(x) + \mu_2(E)f_2(x).$$

Here, $\mu_k(E) \geq 0$, $k = 1, 2$, represent the dependence of the two basis attenuation functions on the energy of the X-rays, and f_k , $k = 1, 2$, are density-like functions. The latter reflect some intrinsic properties of the medium to which X-rays are sensitive and which are independent of energy. Typically, they reflect the mass density (or electron density) and effective atomic number Z_{eff} of the medium.

It turns out that model (1.4) is highly accurate in most applications (both medical and nonmedical). The model was originally proposed in [4] and has since become known as the Alvarez–Macovski dual-energy model. After its publication, the model became widely accepted. See [3, 17, 23, 30, 31] and the references therein, which are a small sample of the large body of literature that utilizes the model. At present, (1.4) is the only widely accepted model to account for the dependence of the X-ray attenuation coefficient μ on energy, which is used by practitioners for image reconstruction in the vast majority of cases.

In some cases, (1.4) is modified to include more terms $\mu_k(E)f_k(x)$. For example, a patient undergoing CT may be injected with a contrast agent that contains high atomic number (high- Z) substances such as iodine ($Z = 53$) and/or gadolinium ($Z = 64$). The attenuation coefficients $\mu(E)$ of these elements exhibit a sharp discontinuity (known as the K-edge discontinuity) at energies relevant to medical X-ray imaging. The presence of the K-edge in the data requires the addition of more terms to the model (1.4) [2, 17, 27]. In this paper we only consider (1.4) with two terms, but our methods can be easily adapted to models with any number of basis functions (see Remark 2.3 and Remark 4.1).

Reconstructing an accurate artifact-free image from data (1.1) is difficult. This follows from the fact that the energy dependence of $\mu(x, E)$ is averaged over all energies in the X-ray beam. Reducing BHA requires complicated processing. Customized algorithms for BHA correction have been developed; however, they have drawbacks and are only guaranteed to work under specific circumstances [7, 28, 29]. Frequently, beam hardening is ignored, and it is assumed that the reconstructed image represents the attenuation coefficient at an effective energy, $\mu(x, E_{\text{eff}})$.

Consequently, the fact that CT data are not line integrals represents the following important question that is not yet fully resolved. What is the nature of the reconstructed image and, more precisely, of image artifacts when conventional Radon transform inversion is applied to the data (1.1)?

Two early papers containing a semi-heuristic analysis of nonlinear effects in CT are [20, 21]. An important step towards rigorously answering this question is made in [22]. The authors propose a model based on the following approximations:

- (1) The source spectrum is confined to a narrow interval $[E_0 - \epsilon, E_0 + \epsilon]$.
- (2) The materials in the object are classified as metal and non-metals.
- (3) The attenuation coefficient of the non-metals is approximately constant in this interval, while the attenuation coefficient of the metal is approximately linear in the interval.

Hence, the attenuation coefficient is approximated by

$$(1.5) \quad \mu(x, E) = \mu(x, E_0) + \alpha(E - E_0)\chi_D, \quad |E - E_0| \leq \epsilon,$$

where D is the support of the metal object and χ_D is the characteristic function of D . Under the above assumptions, the following nonlinear model

for CT data g is derived in [22]:

$$(1.6) \quad \begin{aligned} g &= -\ln \left[\int_{E_0-\epsilon}^{E_0+\epsilon} \rho(E) \exp(-R\mu(\cdot, E)dx) dE \right] \\ &\approx R\mu(\cdot, E_0) - \ln \left(\frac{\sinh(\alpha\epsilon R\chi_D)}{\alpha\epsilon R\chi_D} \right). \end{aligned}$$

The authors also perform a microlocal analysis of artifacts caused by nonlinearities in the data in the framework of their model. Subsequent microlocal analyses of the BHA, namely streaks, under the assumption of the same model are in [6, 19, 32, 33]. The main finding in these papers is that the data g is locally a paired Lagrangian distribution, and this is the root cause of the streaks in the reconstructed image.

While the results obtained by analyzing the model (1.6) are valuable, their utility is limited by the fact that the model's underlying assumptions may not hold. As the preceding discussion shows, assumptions (1) and (3) are not satisfied in the majority of CT scans.

In this paper we study streak artifacts in CT by using the original, most accurate and widely used by practitioners model (1.4). Assuming the model (1.4), the so-called after logs CT data, $g(\mathbf{p})$, $\mathbf{p} = (\alpha, p)$, are

$$(1.7) \quad \begin{aligned} g(\mathbf{p}) &= -\ln G(\mathbf{p}), \quad \mathbf{p} \in M := S^1 \times \mathbb{R}, \\ G(\mathbf{p}) &:= \int_0^{E_{\max}} \rho(E) \exp(-[\mu_1(E)\hat{f}_1(\mathbf{p}) + \mu_2(E)\hat{f}_2(\mathbf{p})]) dE. \end{aligned}$$

Here $\hat{f}_k = Rf_k$ is the classical Radon transform (CRT) of f_k , $k = 1, 2$. Clearly, $g(\alpha, p) = g(\alpha + \pi, -p)$.

Even though (1.7) is quite different from (1.6), there are major similarities in the analyses of the two models and in the main conclusions. We also show that the root cause of the streaks is data nonlinearity, which renders g a paired Lagrangian distribution. Hence, we can use some of the intermediate results obtained in [19, 32, 33]. Nevertheless, our approach differs from these papers. There, the authors (1) approximate the analytic functions $\ln(t)$ and $\sinh(t)$ in (1.6) by polynomials, and then (2) study the singularities of g by analyzing the *approximate* map $\mu \rightarrow g$ using the notion of paired Lagrangian distributions.

Instead, we characterize the singularities of g using the approach developed in [1, 25, 26]. This allows us to study the singularities of the function, f^{rec} , reconstructed from g in a much easier fashion. In particular, no approximation of the model in (1.7) is required. Besides using a more accurate model and a different method of analysis, we also explicitly compute the leading singularity of f^{rec} near the beam hardening streaks. This allows us to characterize streaks more precisely than by computing the order of the distribution. A somewhat similar approach was used in [32] for a related problem.

Interestingly, the model (1.7) has already been used for rigorous analysis of tomographic image reconstruction. See [5], where the authors prove the uniqueness of reconstruction from dual energy data.

Let \mathcal{S} be a piecewise smooth curve without self-intersections with finitely many disconnected components. We assume that $\text{sing supp}(f_k) \subset \mathcal{S}$, $k =$

1, 2. The remainder of this paper is organized as follows. In section 2 we discuss the problem setting. In section 3 we formulate our main result, Theorem 3.1. We also describe qualitatively the singularities of f^{rec} that appear because of data nonlinearity. The proof of Theorem 3.1 is spread over several sections. In section 4 we describe the singularities of g corresponding to smooth sections of \mathcal{S} . In section 5 we describe the singularities of g corresponding to a corner of \mathcal{S} . In section 6 we finish the proof of Theorem 3.1. In sections 7 and 8 we obtain the leading singular behavior of f^{rec} in a neighborhood of streaks caused by data nonlinearity. Finally, in section 9 we conduct a numerical experiment to validate our description of beam hardening streaks in f^{rec} .

2. PROBLEM SETTING

2.1. Assumptions. We begin by describing our assumptions about the f_k . Suppose there are $J \in \mathbb{N}$ bounded domains, $D_j \subset \mathbb{R}^2$, $j = 1, 2, \dots, J$, in the plane. Their boundaries, $S_j := \partial D_j$, are piecewise smooth and disjoint, $S_j \cap S_k = \emptyset$, $j \neq k$. No assumption about the convexity of the D_j 's is made. Denote $\mathcal{S} := \cup_{j=1}^J S_j$. If \mathcal{S} is nonsmooth at x , then x is a corner point of \mathcal{S} and the two one-sided tangents to \mathcal{S} at x do not coincide. Given $x \in \mathcal{S}$ where \mathcal{S} is smooth, $\kappa(x)$ denotes the curvature of \mathcal{S} at x .

Definition 2.1. A line L is tangent to \mathcal{S} at x in the *generalized* sense if L is tangent to \mathcal{S} in the conventional sense if \mathcal{S} is smooth at x or contains x if x is a corner of \mathcal{S} .

Definition 2.2. A line L is called *exceptional* if it is tangent to \mathcal{S} at a point x where $\kappa(x) = 0$ or if it is a one-sided tangent at a corner point of \mathcal{S} .

We suppose that (1) no exceptional line is tangent to \mathcal{S} in the generalized sense at another point, and (2) no line is tangent to \mathcal{S} in the generalized sense at more than two points.

Finally, we suppose there are functions $f_{kj} \in C^\infty(\mathbb{R}^2)$ such that

$$(2.1) \quad f_k = \sum_{j=1}^J f_{k,j} \chi_j, \quad k = 1, 2,$$

where χ_j denotes the characteristic function of D_j . Therefore, $WF(f_k) \subset N^*\mathcal{S}$.

Remark 2.3. The model (2.1) reflects the common assumption that the object being scanned can be segmented into distinct regions D_j , such that the material composition of the object varies smoothly within each region and may change abruptly from one region to another. Hence it is reasonable to assume that, regardless of the number of basis functions, all the f_k 's are smooth within each region and may be discontinuous across region boundaries. Therefore, the assumption that $\text{sing supp } f_k \subset \mathcal{S}$ for all k is practically reasonable.

Throughout the paper, we use the following convention. Let I be a space of distributions, for example, conormal or paired Lagrangian distributions. Recall that $\mathbf{p} = (\alpha, p)$ and $M = S^1 \times \mathbb{R}$ (see (1.7)). We say that $g \in I$ near

\mathfrak{p}_0 (or in an open set M_0) when $\chi g \in I$ for any $\chi \in C^\infty(M)$ supported in a sufficiently small neighborhood of \mathfrak{p}_0 (or supported in M_0). Likewise, given a set $\Xi \subset T^*M$, we say that $WF(g) \in \Xi$ near \mathfrak{p}_0 (or, in an open set M_0) if $WF(\chi g) \in \Xi$ for any χ as above.

2.2. Spaces of symbols and distributions. Let $U \subset \mathbb{R}^n$ be an open set. We say that $a \in S^r(U \times \mathbb{R}^N)$ is the standard symbol of order $r \in \mathbb{R}$ if for any compact $K \subset U$,

$$(2.2) \quad |\partial_x^\beta \partial_\xi^\gamma a(x, \xi)| \leq C_{\beta, \gamma, K} (1 + |\xi|)^{r - |\gamma|}, \quad x \in K, \xi \in \mathbb{R}^N, \beta \in \mathbb{N}_0^N, \gamma \in \mathbb{N}_0^N.$$

Here $\mathbb{N}_0 = 0 \cup \mathbb{N}$. Let $\Lambda \subset T^*U$ be a closed conic Lagrangian submanifold. Suppose Λ is parameterized by a homogeneous phase function $\phi : U \times \mathbb{R}^N \rightarrow \mathbb{R}$:

$$(2.3) \quad \Lambda = \{(x, d_x \phi(x, \xi)) \in T^*U : d_\xi \phi(x, \xi) = 0\}.$$

Then the oscillatory integral

$$(2.4) \quad u(x) = \int_{\mathbb{R}^N} a(x, \xi) e^{i\phi(x, \xi)} d\xi, \quad x \in U,$$

where $a \in S^r(U \times \mathbb{R}^N)$ defines a Lagrangian distribution $u \in I^q(\Lambda)$ of order $q = r - (n/4) + (N/2)$. If $\mathcal{S} \subset U$ is a smooth submanifold and $\Lambda = N^*\mathcal{S}$ is the conormal bundle of \mathcal{S} , then u is a conormal distribution: $u \in I^q(U; \mathcal{S})$ [13, Section 18.2] and [14, Section 25.1].

Suppose $U = U_1 \times U_2$, where $U_j \subset \mathbb{R}^{n_j}$, $x = (x_1, x_2)$, $x_j \in \mathbb{R}^{n_j}$, $j = 1, 2$, and $n = n_1 + n_2$. Then a Lagrangian distribution $u \in I^q(\Lambda)$ defines a Fourier Integral Operator (FIO) $\mathcal{U} : C_0^\infty(U_2) \rightarrow \mathcal{D}'(U_1)$, $\mathcal{U} \in I^q(U_1 \times U_2, \Lambda)$, of order q by the formula

$$(2.5) \quad (\mathcal{U}f)(x_1) = \int_{\mathbb{R}^N} \int_{U_2} a(x, \xi) e^{i\phi(x, \xi)} f(x_2) dx_2 d\xi, \quad x_1 \in U_1.$$

See [14, Section 25.2].

Suppose that two Lagrangian submanifolds $\Lambda_0, \Lambda_1 \subset T^*U$ intersect transversally at a codimension k submanifold Ω . The space of paired Lagrangian distributions of order p, l , denoted $I^{p, l}(\Lambda_0, \Lambda_1)$, is the set of distributions u that satisfy $u \in I^{p+ l}(\Lambda_0 \setminus \Omega)$ and $u \in I^p(\Lambda_1 \setminus \Omega)$, see [12, 18] for more details.

2.3. Preliminaries. Pick any $x_0 \in \mathcal{S}$. Let U be a small neighborhood of x_0 . As is well known, $f_k \in I^{-1}(U; \mathcal{S})$ if $\mathcal{S} \cap U$ is smooth. If x_0 is a corner of \mathcal{S} , we assume $\mathcal{S} \cap U = \mathcal{S}_1 \cup \mathcal{S}_2$, where $\mathcal{S}_{1,2}$ are smooth curve segments that share a common endpoint, x_0 (see Figure 3, left panel). In this case

$$(2.6) \quad f_k \in I^{-1, -1/2}(N^*x_0; \mathcal{S}_1) + I^{-1, -1/2}(N^*x_0; \mathcal{S}_2)$$

near x_0 [19, Lemma 5.1].

The CRT $R : \mathcal{E}(\mathbb{R}^2) \rightarrow \mathcal{D}(M)$ is an elliptic FIO given by

$$(2.7) \quad \hat{f}(\mathfrak{p}) = \int_{\mathbb{R}^2} f(x) \delta(\vec{\alpha} \cdot x - p) dx = \frac{1}{2\pi} \int_{\mathbb{R}} \int_{\mathbb{R}^2} f(x) e^{i\lambda(\vec{\alpha} \cdot x - p)} dx d\lambda.$$

This implies that the CRT is an FIO of order $q = 0 - (n/4) + (k/2) = -1/2$, where $n = 4$ and $k = 1$. The ambient space here is $M \times \mathbb{R}^2$, and thus, its

dimension is $n = 4$. The canonical relation of the CRT is

$$(2.8) \quad C = \{((\alpha, p), \lambda(\vec{\alpha}^\perp \cdot x, -1)); (x, -\lambda\vec{\alpha})\} : \\ (\alpha, p) \in M, x \in \mathbb{R}^2, \vec{\alpha} \cdot x - p = 0, \lambda \in \mathbb{R} \setminus 0\} \subset T^*M \setminus 0 \times T^*\mathbb{R}^2 \setminus 0.$$

Clearly, C is a homogeneous canonical relation. A CRT inversion formula is as follows:

$$(2.9) \quad f(x) = (R^{-1}\hat{f})(x) = -\frac{1}{2\pi^2} \int_0^\pi \int_{\mathbb{R}} \frac{\partial_p g(\alpha, p)}{p - \vec{\alpha} \cdot x} dp d\alpha = -\frac{1}{2\pi} (R^* \mathcal{H} \partial_p f)(x),$$

where \mathcal{H} denotes the Hilbert transform. This is also an elliptic FIO, and its homogeneous canonical relation, C^* , is obtained from C in (2.8) by swapping the coordinates:

$$(2.10) \quad C^* = \{((x, \xi); (\mathbf{p}, \eta)) : ((\mathbf{p}, \eta); (x, \xi)) \in C\} \subset T^*\mathbb{R}^2 \setminus 0 \times T^*M \setminus 0.$$

It is clear from (2.8) and (1.7) that

$$(2.11) \quad \begin{aligned} & \text{sing supp}(\hat{f}_k), \text{sing supp}(g) \subset \Gamma, \\ & \Gamma = \{(\alpha, p) \in M : (x, \vec{\alpha}) \in N^*\mathcal{S}, p = \vec{\alpha} \cdot x\}. \end{aligned}$$

Put simply, $\mathbf{p} \in \Gamma$ if $L_{\mathbf{p}} := \{x \in \mathbb{R}^2 : \vec{\alpha} \cdot x = p\}$ is tangent to \mathcal{S} in the generalized sense. Thus, Γ is the generalized Legendre transform of \mathcal{S} [26]. We denote this relation by $\Gamma = \mathcal{L}(\mathcal{S})$. The generalized Legendre transform is very closely related to the Legendre-Fenchel transform [8, Chapter VI].

3. MAIN RESULTS

We now state our main results.

Theorem 3.1. *Let $f_{1,2}$ and \mathcal{S} satisfy the assumptions in section 2.1. Select some $\mathbf{p}_0 \in \Gamma$ and let M_0 be a sufficiently small neighborhood of \mathbf{p}_0 . One has*

- (1) *sing supp(g) $\subset \Gamma$.*
- (2) *If Γ is nonsmooth at \mathbf{p}_0 , then $L_{\mathbf{p}_0}$ is tangent to \mathcal{S} at an isolated point where the curvature of \mathcal{S} equals zero.*
- (3) *If Γ self-intersects at \mathbf{p}_0 , i.e. $\Gamma \cap M_0 = \Gamma_1 \cup \Gamma_2$ for some smooth $\Gamma_{1,2}$, then $L_{\mathbf{p}_0}$*
 - (a) *is tangent to \mathcal{S} at two different points, or*
 - (b) *contains a line segment of \mathcal{S} , or*
 - (c) *is a one-sided tangent to \mathcal{S} at a corner point.**In cases (a) and (b), Γ_1 and Γ_2 are transversal at \mathbf{p}_0 , and Γ_1 and Γ_2 are tangent at \mathbf{p}_0 in case (c).*
- (4) *If $\Gamma \cap M_0$ is a smooth curve without self-intersections, then $\hat{f}_k \in I^{-r}(M_0; \Gamma)$, $k = 1, 2$, implies $g \in I^{-r}(M_0; \Gamma)$. Here $r = 3/2$ if $L_{\mathbf{p}_0}$ passes through a corner of \mathcal{S} and $r = 2$ if $L_{\mathbf{p}_0}$ is tangent to \mathcal{S} .*
- (5) *Suppose $\Gamma \cap M_0 = \Gamma_1 \cup \Gamma_2$, where $\Gamma_{1,2}$ are smooth and intersect transversely at \mathbf{p}_0 . Because of nonlinear interaction, g is a paired Lagrangian distribution near \mathbf{p}_0 :*

$$(3.1) \quad g \in I^{-r_1, -r_2+(1/2)}(N^*\mathbf{p}_0, N^*\Gamma_1) + I^{-r_2, -r_1+(1/2)}(N^*\mathbf{p}_0, N^*\Gamma_2).$$

Here $r_j = 3/2$ in the case of the usual tangency at x_j and $r_j = 2$ if x_j is a corner point, $j = 1, 2$.

- (6) Let M' be the finite collection of all $\mathbf{p} \in M$ such that either Γ is nonsmooth at \mathbf{p} or self-intersects at \mathbf{p} . Then

$$(3.2) \quad WF(g) \subset N^*(\Gamma \setminus M') \cup \left(\bigcup_{\mathbf{p} \in M'} N^*\mathbf{p} \right).$$

Let us briefly discuss the above six claims. The first three are about the geometric properties of the singular support of g , Γ , and how they relate to the geometric properties of \mathcal{S} . The last three claims provide a microlocal description of the singularities of g .

Claim (1) states that the singular support of g does not extend beyond Γ , the singular support of \hat{f}_k 's. Claims (2) and (3) are well-known properties of the Legendre transform. We state and prove them to make the proofs of the other claims self-contained. Claim (4) asserts that if $\Gamma \cap M_0$ is smooth, then g and \hat{f}_k are locally conormal distributions of the same order.

Claim (5) states that if $\Gamma \cap M_0 = \Gamma_1 \cap \Gamma_2$ and the intersection is transversal, then g is a paired Lagrangian distribution with the given orders. Such a shape of Γ occurs near a point \mathbf{p}_0 if $L_{\mathbf{p}_0}$ is a double tangent to \mathcal{S} . See, e.g., Figure 1.

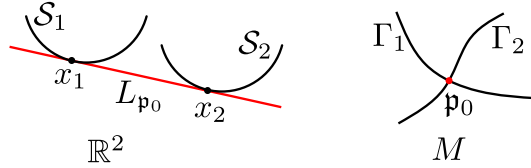


FIGURE 1. The case when local segments of \mathcal{S} near x_1 and x_2 are on one side of the double tangent $L_{\mathbf{p}_0}$.

Claims (4) and (5) do not address the following two cases: (1) Γ is non-smooth at \mathbf{p}_0 ; and (2) $\Gamma \cap M_0 = \Gamma_1 \cap \Gamma_2$ and $\Gamma_{1,2}$ are tangent to each other at \mathbf{p}_0 . Claim (6) states that, at worst, this singular behavior of Γ at $\mathbf{p}_0 \in M'$ adds $N^*\mathbf{p}_0$ to $WF(g)$. We do not study these two cases in more detail because they are not related to data nonlinearity.

Since R^{-1} is an FIO with the canonical relation given in (2.10), (3.2) gives

$$(3.3) \quad WF(f^{\text{rec}}) \subset N^*\mathcal{S} \cup \left(\bigcup_{\mathbf{p} \in M'} N^*L_{\mathbf{p}} \right).$$

In other words, whenever $N^*\mathbf{p}$ appears in $WF(g)$, it may cause a streak along $L_{\mathbf{p}}$ in f^{rec} . The reason $N^*\mathbf{p}$ appears in $WF(g)$ (or does not appear) can be different. To better understand the implications of (3.3), we identify the following three groups of cases.

- (1) Γ is locally smooth (claim (4) of Theorem 3.1). In this case, no singularities are added to f^{rec} .
- (2) Locally, $\Gamma = \Gamma_1 \cap \Gamma_2$, where Γ_j are smooth and intersect transversely at \mathbf{p}_0 (claim (5) of Theorem 3.1). In this case, the component $N^*\mathbf{p}_0 \subset WF(g)$ appears owing to *nonlinear interaction*. This can cause a streak along $L_{\mathbf{p}_0}$ in f^{rec} .
- (3) Exceptional cases: Γ is not smooth or $\Gamma = \Gamma_1 \cap \Gamma_2$, where Γ_j are smooth and tangent to each other at some $\mathbf{p} \in M$ (all the remaining

cases in claim (6) of Theorem 3.1). The component $N^*\mathbf{p} \subset WF(g)$ also appears in this case, leading to a possible streak along $L_{\mathbf{p}}$ in f^{rec} . However, the root cause of the streak is not the nonlinearity of the data measurement, but the fact that g is not in the range of R .

See also [20, 21], where cases (2) and (3), which describe artifacts, are identified using heuristic arguments.

4. SINGULARITIES OF DATA – LOCALLY SMOOTH \mathcal{S}

Our first goal is to describe the behavior of $g(\mathbf{p})$ near its singular support. Select some $\mathbf{p}_0 = (\alpha_0, p_0) \in \Gamma$ and consider the line $L_{\mathbf{p}_0}$. Suppose $L_{\mathbf{p}_0}$ is tangent to \mathcal{S} at some point x_0 , $\varkappa(x_0) \neq 0$. Let $p = P(\alpha)$ be a parameterization of Γ in a neighborhood of \mathbf{p}_0 . The assumption $\varkappa(x_0) \neq 0$ implies that both Γ and $P(\alpha)$ are locally smooth. It is easy to establish that

$$(4.1) \quad \begin{aligned} \hat{f}_k(\mathbf{p}) &= (p - P(\alpha))_\iota^{1/2} R_k(\mathbf{p}) + T_k(\mathbf{p}), \quad \mathbf{p} \in M_0, \\ R_k(\mathbf{p}_0) &= 2(2/\varkappa(x_0))^{1/2}, \end{aligned}$$

where $\iota = +$ or $-$ (depending on the location of \mathcal{S} relative to $L_{\mathbf{p}_0}$), $t_\iota = \max(0, \iota t)$, $M_0 = I_\alpha \times I_p$ is a sufficiently small, rectangular neighborhood of \mathbf{p}_0 , $R_k, T_k \in C^\infty(M_0)$, and $P \in C^\infty(I_\alpha)$ [1, 25, 26].

4.1. Tangency at a single point. Suppose $L_{\mathbf{p}_0}$ is tangent to \mathcal{S} *only at one point*, x_0 , and $L_{\mathbf{p}_0}$ is not tangent to \mathcal{S} in the generalized sense at another point. We substitute (4.1) into (1.7). Expand e^t at $t = 0$ in the Taylor series and group the terms to get

$$(4.2) \quad G(\mathbf{p}) = (p - P(\alpha))_\iota^{1/2} A_{1/2}(\mathbf{p}) + (p - P(\alpha))_\iota A_1(\mathbf{p}) + G_0(\mathbf{p}), \quad \mathbf{p} \in M_0,$$

where $A_{1/2}, A_1, G_0 \in C^\infty(M_0)$. These functions are given by

$$(4.3) \quad \begin{aligned} A_{1/2}(\mathbf{p}) &= - \sum_{n \geq 1, n \text{ odd}} \frac{G_n(\mathbf{p})}{n!} (p - P(\alpha))^{(n-1)/2}, \\ A_1(\mathbf{p}) &= \sum_{n \geq 2, n \text{ even}} \frac{G_n(\mathbf{p})}{n!} (p - P(\alpha))^{(n-2)/2}, \\ G_n(\mathbf{p}) &= \int_0^{E_{\text{mx}}} W(E, \mathbf{p}) [\mu_1(E) R_1(\mathbf{p}) + \mu_2(E) R_2(\mathbf{p})]^n dE, \\ W(E, \mathbf{p}) &= \rho(E) \exp(-[\mu_1(E) T_1(\mathbf{p}) + \mu_2(E) T_2(\mathbf{p})]). \end{aligned}$$

The two series converge absolutely because $|G_n(\mathbf{p})| \leq c^n$, $\mathbf{p} \in M_0$, for some $c > 0$.

Substituting (4.2) into the first equation in (1.7) yields

$$(4.4) \quad \begin{aligned} g &= -\ln(G_0 + (p - P(\alpha))_\iota^{1/2} A_{1/2} + (p - P(\alpha))_\iota A_1) \\ &= -\ln G_0 + \sum_{n \geq 1} \frac{(-1)^n}{n} \frac{[(p - P(\alpha))_\iota^{1/2} A_{1/2} + (p - P(\alpha))_\iota A_1]^n}{G_0^n}, \end{aligned}$$

where we dropped \mathbf{p} from the arguments of all functions. We assume that there is no photon starvation, that is,

$$(4.5) \quad \inf_{\mathbf{p} \in M_0} \|W(\cdot, \mathbf{p})\|_{L^\infty([0, E_{\text{mx}}])} > 0.$$

In this case, $\inf_{\mathbf{p} \in M_0} G_0(\mathbf{p}) > 0$. Clearly, the series in (4.4) converges absolutely provided $\iota(p - P(\alpha)) > 0$ is sufficiently small. If $\iota(p - P(\alpha)) \leq 0$, then the series vanishes. Therefore,

$$(4.6) \quad g(\mathbf{p}) = -\ln G_0(\mathbf{p}) + (p - P(\alpha))_{\iota}^{1/2} B_{1/2}(\mathbf{p}) + (p - P(\alpha))_{\iota} B_1(\mathbf{p}), \quad \mathbf{p} \in M_0,$$

for some $B_r \in C^\infty(M_0)$, $r \in \{1/2, 1\}$. In particular, by (4.3),

$$(4.7) \quad B_{1/2} = \frac{G_1}{G_0} = \frac{\int_0^{E_{\max}} W(E) [\mu_1(E) R_1 + \mu_2(E) R_2] dE}{\int_0^{E_{\max}} W(E) dE}, \quad p = P(\alpha), \alpha \in I_\alpha.$$

As is easily seen from (4.1) and (4.6),

$$(4.8) \quad \hat{f}_k, g \in I^{-3/2}(M_0; \Gamma)$$

are conormal distributions. The claim regarding \hat{f}_k is well known. Since

$$(4.9) \quad \mathcal{F}(t_\pm^{1/2}) = O(|\lambda|^{-3/2}), \quad \lambda \rightarrow \infty,$$

(see (7.3) and (8.2)), the order of the conormal distributions \hat{f}_k and g is $q = (-3/2) + (n/4) - (k/2) = -3/2$. Here, $n = 2$ is the dimension of the ambient space \mathbb{R}^2 , and $k = 1$ is the dimension of the dual variable λ .

4.2. Tangency at two points. Next, suppose $L_{\mathbf{p}_0}$ is tangent to \mathcal{S} at two points $x_1 \neq x_2$ (see Figure 1). Let \mathcal{S}_j be a local segment of \mathcal{S} in a neighborhood of x_j , $j = 1, 2$. We assume that $\mathcal{S}_{1,2}$ are smooth and $\varkappa(x_j) \neq 0$, $j = 1, 2$. Further, $\Gamma \cap M_0 = \Gamma_1 \cup \Gamma_2$, where $\Gamma_j = \mathcal{L}(\mathcal{S}_j)$. Additionally, Γ_1 and Γ_2 intersect transversely at \mathbf{p}_0 [19]. Let $p = P_j(\alpha)$ be a local parameterization of Γ_j . Then $p_0 = P_1(\alpha_0) = P_2(\alpha_0)$. The analog of (4.1) becomes

$$(4.10) \quad \begin{aligned} \hat{f}_k(\mathbf{p}) &= (p - P_j(\alpha))_{\iota_j}^{1/2} R_{k,j}(\mathbf{p}) + T_{k,j}(\mathbf{p}), \quad \mathbf{p} \in M_0, \\ R_{k,j}(\mathbf{p}_0) &= 2(2/\varkappa(x_j))^{1/2}, \quad j = 1, 2. \end{aligned}$$

Substituting (4.10) into (1.7) gives

$$(4.11) \quad G(\mathbf{p}) = \sum_{m,n \geq 0} \frac{(-1)^{m+n}}{m!n!} G^{(m,n)}(\mathbf{p}), \quad \mathbf{p} \in M_0,$$

where the series converges absolutely and

$$(4.12) \quad \begin{aligned} G^{(m,n)} &:= \int_0^{E_{\max}} W(E) [(p - P_1)_{\iota_1}^{1/2} (\mu_1(E) R_{1,1} + \mu_2(E) R_{2,1})]^m \\ &\quad \times [(p - P_2)_{\iota_2}^{1/2} (\mu_1(E) R_{1,2} + \mu_2(E) R_{2,2})]^n dE, \\ W(E) &= \rho(E) \exp [-\mu_1(E)(T_{1,1} + T_{1,2}) - \mu_2(E)(T_{2,1} + T_{2,2})]. \end{aligned}$$

For simplicity, we removed the arguments α and p from all the functions in the above equation. Expanding further and combining terms gives

$$\begin{aligned}
 G(\mathbf{p}) = & A_{0,0}(\mathbf{p}) + \sum_{s_1 \in \{1/2, 1\}} G_{s_1,0}(\mathbf{p}) + \sum_{s_2 \in \{1/2, 1\}} G_{0,s_2}(\mathbf{p}) \\
 & + \sum_{s_1, s_2 \in \{1/2, 1\}} G_{s_1, s_2}(\mathbf{p}), \quad \mathbf{p} \in M_0, \\
 G_{s_1, s_2}(\mathbf{p}) := & (p - P_1(\alpha))_{\iota_1}^{s_1} (p - P_2(\alpha))_{\iota_2}^{s_2} A_{s_1, s_2}(\mathbf{p}), \\
 A_{0,0}(\mathbf{p}) = & \int_0^{E_{\max}} W(E, \mathbf{p}) dE,
 \end{aligned} \tag{4.13}$$

where $A_{s_1, s_2} \in C^\infty(M_0)$.

As in the preceding subsection, if there is no photon starvation, then

$$\inf_{\mathbf{p} \in M_0} A_{0,0}(\mathbf{p}) > 0. \tag{4.14}$$

Expand $\ln t$ in a series at $t = 1$ to get

$$\begin{aligned}
 g(\mathbf{p}) = & B_{0,0}(\mathbf{p}) + \sum_{s_1 \in \{1/2, 1\}} (p - P_1(\alpha))_{\iota_1}^{s_1} B_{s_1,0}(\mathbf{p}) \\
 & + \sum_{s_2 \in \{1/2, 1\}} (p - P_2(\alpha))_{\iota_2}^{s_2} B_{0,s_2}(\mathbf{p}) \\
 & + \sum_{s_1, s_2 \in \{1/2, 1\}} (p - P_1(\alpha))_{\iota_1}^{s_1} (p - P_2(\alpha))_{\iota_2}^{s_2} B_{s_1, s_2}(\mathbf{p}), \\
 B_{0,0}(\mathbf{p}) = & -\ln(A_{0,0}(\mathbf{p})), \quad \mathbf{p} \in M_0,
 \end{aligned} \tag{4.15}$$

where $B_{s_1, s_2} \in C^\infty(M_0)$, $s_1, s_2 \in \{0, 1/2, 1\}$. In particular, setting $\mathbf{p} = \mathbf{p}_0$ gives

$$\begin{aligned}
 B_{\frac{1}{2}, \frac{1}{2}} &= A_{\frac{1}{2}, \frac{1}{2}} / A_{0,0} \\
 &= \frac{\int_0^{E_{\max}} W(E) [\mu_1(E) R_{1,1} + \mu_2(E) R_{2,1}] [\mu_1(E) R_{1,2} + \mu_2(E) R_{2,2}] dE}{\int_0^{E_{\max}} W(E) dE}.
 \end{aligned} \tag{4.16}$$

By (4.15),

$$g \in I^{-3/2, -1}(N^* \mathbf{p}_0, N^* \Gamma_1) + I^{-3/2, -1}(N^* \mathbf{p}_0, N^* \Gamma_2) \tag{4.17}$$

near \mathbf{p}_0 .

To explain the values $p = -3/2$ and $l = -1$ for the superscripts of $I^{p,l}$ in (4.17), note that $g \in I^{-3/2}(N^* \Gamma_j \setminus N^* \mathbf{p}_0)$, $j = 1, 2$, by (4.8). Therefore $p = -3/2$. The value of l is computed from the requirement $g \in I^{-3/2}(N^* \mathbf{p}_0 \setminus N^* \Gamma_j)$. Hence, we solve $p + l = -3 - (n/4) + (k/2)$. The number -3 in this equation appears because each factor $(p - P_j(\alpha))_{\iota_j}^{1/2}$ contributes a decay of order $-3/2$ in the Fourier domain, and we take $k = 2$ because this is the dimension of the Fourier integral representing the product $(p - P_1(\alpha))_{\iota_1}^{1/2} (p - P_2(\alpha))_{\iota_2}^{1/2}$.

Remark 4.1. Equation (4.15) also holds for models of the kind (1.4) with more basis functions $\mu_k(E) f_k(x)$, $k = 1, 2, \dots, K$, as long as $\text{sing supp } f_k \in \mathcal{S}$

for all k . The only difference is that the formulas for the coefficients A_{s_1, s_2} involve more terms (cf. (4.12) and (4.13)).

5. CORNER CASES.

Suppose \mathcal{S} has a corner at x_0 , i.e. one-sided tangents to \mathcal{S} at x_0 , $L_{\mathbf{p}_1}$ and $L_{\mathbf{p}_2}$, do not coincide (see Figure 3). Pick $\mathbf{p}_0 \in M$, $\mathbf{p}_0 \neq \mathbf{p}_{1,2}$, such that $x_0 \in L_{\mathbf{p}_0}$. As before, let M_0 be a sufficiently small neighborhood of \mathbf{p}_0 . It is easily seen that, if $L_{\mathbf{p}_0}$ is not tangent to \mathcal{S} elsewhere in the generalized sense, then

$$(5.1) \quad \begin{aligned} \hat{f}_k(\mathbf{p}) &= (p - P(\alpha))_+ R_k^+(\mathbf{p}) + (p - P(\alpha))_- R_k^-(\mathbf{p}) + T_k(\mathbf{p}), \\ P(\alpha) &= \vec{\alpha} \cdot x_0, \quad \mathbf{p} \in M_0, \end{aligned}$$

where $R_k^\pm, T_k \in C^\infty(M_0)$, $k = 1, 2$. Similarly to section 4.1 we find

$$(5.2) \quad g(\mathbf{p}) = -\ln G_0(\mathbf{p}) + (p - P(\alpha))_+ B_+(\mathbf{p}) + (p - P(\alpha))_- B_-(\mathbf{p}), \quad \mathbf{p} \in M_0,$$

for some $G_0, B_\pm \in C^\infty(M_0)$. Clearly,

$$(5.3) \quad \hat{f}_k, g \in I^{-2}(M_0; \Gamma_{x_0}).$$

Here and throughout the paper we denote

$$(5.4) \quad \Gamma_x = \{(\alpha, \vec{\alpha} \cdot x) \in M : \vec{\alpha} \in S^1\}.$$

Similarly to (4.8), the order -2 follows from $\mathcal{F}(t_\pm) = O(|\lambda|^{-2})$, $\lambda \rightarrow \infty$.

Now we consider the general case when $L_{\mathbf{p}_0}$ is tangent to \mathcal{S} in the generalized sense at two points, x_1 and x_2 . See, for example, Figure 4, where the case of two corner points is shown. Then, $\Gamma \cap M_0 = \Gamma_1 \cup \Gamma_2$, Γ_1 and Γ_2 are smooth and intersect transversely at \mathbf{p}_0 . The complete expression for g is too long; therefore, we describe only the relevant paired Lagrangian part:

$$(5.5) \quad \begin{aligned} g(\mathbf{p}) - \sum_{\iota_1, \iota_2 \in \{+, -\}} \sum_{s_1, s_2 \in \{1/2, 1\}} (p - P_1(\alpha))_{\iota_1}^{s_1} (p - P_2(\alpha))_{\iota_2}^{s_2} B_{\iota_1, \iota_2}^{s_1, s_2}(\mathbf{p}) \\ \in I^{-r_1}(M_0; \Gamma_1) + I^{-r_2}(M_0; \Gamma_2) \end{aligned}$$

with some $B_{\iota_1, \iota_2}^{s_1, s_2} \in C^\infty(M_0)$. The values of r_j and s_j depend on the singularity type of f near x_j , $j = 1, 2$. If \mathcal{S} is smooth at x_j , then $r_j = 3/2$ and $s_j \in \{1/2, 1\}$, cf. (4.6) and (4.15). If \mathcal{S} has a corner at x_j , then $r_j = 2$ and $s_j = 1$, cf. (5.2). Furthermore,

$$(5.6) \quad g \in I^{-r_1, -r_2 + (1/2)}(N^* \mathbf{p}_0, N^* \Gamma_1) + I^{-r_2, -r_1 + (1/2)}(N^* \mathbf{p}_0, N^* \Gamma_2)$$

in M_0 . The orders p and l are computed similarly to (4.17) using (4.8) and (5.3).

6. END OF PROOF OF THEOREM 3.1

Claim (1) is proven in (2.11). To prove claims (2)–(6), we review several cases.

1. \mathcal{S} is smooth at x_0 , $\varkappa(x_0) \neq 0$, and $L_{\mathbf{p}_0}$ is tangent to \mathcal{S} only at x_0 . As is well known, in this case $\Gamma \cap M_0$ is smooth and $\hat{f}_k \in I^{-3/2}(N^* \Gamma)$ is a conormal distribution near \mathbf{p}_0 , $k = 1, 2$. From (4.6), g is also a conormal distribution, and $g \in I^{-3/2}(N^* \Gamma)$ near \mathbf{p}_0 .

2. $L_{\mathbf{p}_0}$ is tangent to \mathcal{S} at x_1 and x_2 (and only at these two points), \mathcal{S} is smooth in a neighborhood of x_1, x_2 , and $\varkappa(x_k) \neq 0$, $k = 1, 2$, see Figure 1. Let \mathcal{S}_k be a local segment of \mathcal{S} near x_k and $\Gamma_k := \mathcal{L}(\mathcal{S}_k) \cap M_0$, $k = 1, 2$. Then $\Gamma_1 \cap \Gamma_2 = \mathbf{p}_0$ and the intersection is transversal [19, p. 4920].

In the linear Radon transform framework, the singularities at Γ_1 and Γ_2 do not interact. However, the nonlinearity of the measurement leads to an interaction at \mathbf{p}_0 (see (4.15)). As a consequence,

$$(6.1) \quad WF(g) \subset N^*\Gamma_1 \cup N^*\Gamma_2 \cup N^*\mathbf{p}_0$$

near \mathbf{p}_0 . More precisely, (4.15) implies (see also [19, p. 4920]):

$$(6.2) \quad g \in I^{-3/2, -1}(N^*\mathbf{p}_0, N^*\Gamma_1) + I^{-3/2, -1}(N^*\mathbf{p}_0, N^*\Gamma_2).$$

The component $N^*\mathbf{p}_0$ in $WF(g)$ arises owing to the nonlinear interaction of singularities at \mathbf{p}_0 .

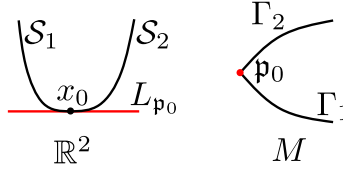


FIGURE 2. The case $\varkappa(x_0) = 0$.

3. \mathcal{S} is smooth near x_0 , $\varkappa(x_0) = 0$ and $L_{\mathbf{p}_0}$ is tangent to \mathcal{S} at x_0 , see Figure 2. According to Definition 2.2, $L_{\mathbf{p}_0}$ is an exceptional line; therefore, it is not tangent to \mathcal{S} elsewhere in the generalized sense. As is easily seen, Γ is non-smooth at \mathbf{p}_0 , i.e. $\Gamma \cap M_0 = \Gamma_1 \cup \Gamma_2$ for some Γ_1 and Γ_2 that are smooth and share an endpoint, \mathbf{p}_0 (see Figure 2, right panel). Then

$$(6.3) \quad WF(\hat{f}_k), WF(g) \subset N^*\Gamma_1 \cup N^*\Gamma_2 \cup N^*\mathbf{p}_0.$$

This implies that the component $N^*\mathbf{p}_0$ of $WF(g)$ arises because of the shape of \mathcal{S} near x_0 and not because of a nonlinear effect.

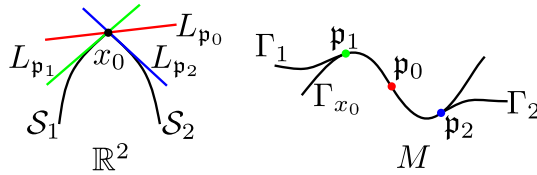


FIGURE 3. One corner case.

4. \mathcal{S} has a corner at x_0 , see Figure 3. Thus, $\mathcal{S} = \mathcal{S}_1 \cup \mathcal{S}_2$ in a neighborhood of x_0 , where $\mathcal{S}_{1,2}$ are smooth curves that share an endpoint, x_0 . Let $L_{\mathbf{p}_j}$ be tangent to \mathcal{S}_j at x_0 , $j = 1, 2$. Pick any $\mathbf{p}_0 \in M$ such that $x_0 \in L_{\mathbf{p}_0}$, $\mathbf{p}_0 \neq \mathbf{p}_{1,2}$, and $L_{\mathbf{p}_0}$ is not tangent to \mathcal{S} in the generalized sense elsewhere. Because $L_{\mathbf{p}_1}$ and $L_{\mathbf{p}_2}$ are one-sided tangents to \mathcal{S} at x_0 , they are exceptional lines and are not tangent to \mathcal{S} in the generalized sense elsewhere either.

Let M_0 be a small neighborhood of $\{\mathbf{p}_0, \mathbf{p}_1, \mathbf{p}_2\}$ and denote $\Gamma_j = \mathcal{L}(\mathcal{S}_j) \cap M_0$, $j = 1, 2$. It is easy to verify that Γ_j is tangent to Γ_{x_0} at \mathbf{p}_j . Then,

$$(6.4) \quad WF(\hat{f}_k) \subset N^*\Gamma_1 \cup N^*\Gamma_2 \cup N^*\Gamma_{x_0} \cup N^*\mathbf{p}_1 \cup N^*\mathbf{p}_2, \quad k = 1, 2,$$

in M_0 . By (4.6) and (5.2),

$$(6.5) \quad \begin{aligned} g &\in I^{-3/2}(M_0; \Gamma_j) \text{ near any } \mathbf{p} \in \Gamma_j \setminus \mathbf{p}_j, \quad j = 1, 2, \\ g &\in I^{-2}(M_0; \Gamma_{x_0}) \text{ near any } \mathbf{p} \in \Gamma_{x_0} \setminus \{\mathbf{p}_1, \mathbf{p}_2\}. \end{aligned}$$

Hence

$$(6.6) \quad WF(g) \subset N^*\Gamma_1 \cup N^*\Gamma_2 \cup N^*\Gamma_{x_0} \cup N^*\mathbf{p}_1 \cup N^*\mathbf{p}_2$$

in M_0 .

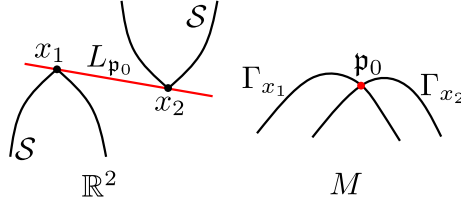


FIGURE 4. $L_{\mathbf{p}_0}$ is tangent to \mathcal{S} in the generalized sense at two corner points.

5. Suppose $L_{\mathbf{p}_0}$ is tangent in the general sense to \mathcal{S} at two points, x_1 and x_2 . The two-corner case is shown in Figure 4. As in case 1, $\Gamma \cap M_0 = \Gamma_1 \cup \Gamma_2$, where $\Gamma_{1,2}$ are smooth and intersect transversely at \mathbf{p}_0 . For example, $\Gamma_j = \Gamma_{x_j}$, $j = 1, 2$, in Figure 4. As before, a nonlinear interaction exists at \mathbf{p}_0 . By (5.5),

$$(6.7) \quad WF(g) \subset N^*\Gamma_1 \cup N^*\Gamma_2 \cup N^*\mathbf{p}_0,$$

and, more precisely,

$$(6.8) \quad g \in I^{-r_1, -r_2 + (1/2)}(N^*\mathbf{p}_0, N^*\Gamma_1) + I^{-r_2, -r_1 + (1/2)}(N^*\mathbf{p}_0, N^*\Gamma_2).$$

where $r_j = 3/2$ in the case of the usual tangency at x_j and $r_j = 2$ if x_j is a corner point, $j = 1, 2$. Both inclusions, (6.7) and (6.8), are understood as holding in a neighborhood of \mathbf{p}_0 .

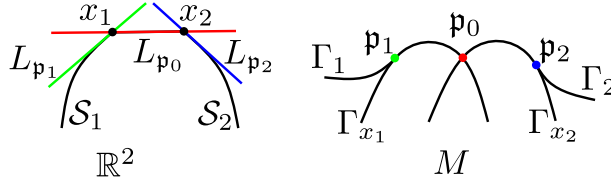


FIGURE 5. The line segment case.

6. \mathcal{S} contains a flat segment whose endpoints, x_1 and x_2 , are corners, see Figure 5. As in case 4, similarly to (6.4),

$$(6.9) \quad WF(\hat{f}_k), WF(g) \subset N^*\Gamma_j \cup N^*\Gamma_{x_j} \cup N^*\mathbf{p}_j, \quad j = 1, 2, \quad k = 1, 2.$$

Let $L_{\mathbf{p}_0}$ be the line that contains the line segment $[x_1, x_2]$. Near \mathbf{p}_0 , we have similarly to (6.8)

$$(6.10) \quad g \in I^{-2, -3/2}(N^*\mathbf{p}_0, N^*\Gamma_{x_1}) + I^{-2, -3/2}(N^*\mathbf{p}_0, N^*\Gamma_{x_2}).$$

This completes the analysis of possible cases. Now, we prove the remaining claims. The above analysis shows that Γ is nonsmooth only in case 3 and self-intersects in cases 2, 3, and 6. This proves claims 2 and 3.

From the above analysis, Γ is locally smooth only if it corresponds to a smooth segment of \mathcal{S} with a nonvanishing curvature or to a corner point (away from one-sided tangents). Hence, cases 1 and 4 prove claim 4.

Claim 5 follows from cases 2, 5, and 6 (see (6.2), (6.8), (6.10)).

Claim 6 follows from the results of all six cases, including (6.1), (6.3), (6.6), (6.7), and (6.9). This completes the proof of Theorem 3.1.

7. STRENGTH OF ADDED SINGULARITIES.

There are no added singularities when L_{p_0} is tangent to \mathcal{S} at only one point where the curvature of \mathcal{S} is nonzero (case 1 in section 6). Similarly, only the last sum in (4.15) contributes to nonlocal artifacts in the case of tangency at two points (case 2 in section 6). Because we use a linear inversion formula, we separately study the contribution of each term. Pick one of them and denote it

$$(7.1) \quad g_a(\alpha, p) = (p - P_1(\alpha))_{\iota_1}^{s_1} (p - P_2(\alpha))_{\iota_2}^{s_2} B(\alpha, p).$$

The subscript ‘ a ’ stands for ‘artifact.’ Because R^{-1} is linear, using a partition of unity, we can assume without loss of generality that $B \in C_0^\infty(M_0)$. The reconstruction from g_a uses (2.9) as follows:

$$(7.2) \quad f_a(x) := (R^{-1}g_a)(x) = -\frac{1}{2\pi^2} \int_0^\pi \int_{\mathbb{R}} \frac{\partial_p g_a(\alpha, p)}{p - \vec{\alpha} \cdot x} dp d\alpha.$$

The values $s_1 = s_2 = 1/2$ produce the strongest singularities; therefore, we consider only this case. The other values of s_1, s_2 can be analyzed in an analogous manner.

We begin by setting $\iota_1 = \iota_2 = +$. The case $\iota_1 = \iota_2 = -$ is completely analogous.

7.1. The ++ case. Using entry 26 in the Table of Fourier Transforms of [11]

$$(7.3) \quad p_+^{1/2} = \frac{\Gamma(3/2)e(-3/2)}{2\pi} \int_{\mathbb{R}} (\lambda - i0)^{-3/2} e^{i\lambda p} d\lambda, \quad e(r) = \exp(ir\pi/2),$$

the 2D Fourier transform of g_a is

$$(7.4) \quad \begin{aligned} \tilde{g}_a(\eta) = & \frac{\Gamma^2(3/2)e(-3)}{(2\pi)^2} \int_{M_0} \int_{\mathbb{R}} \int_{\mathbb{R}} (\lambda - i0)^{-3/2} (\mu - i0)^{-3/2} B(\alpha, p) \\ & \times e^{i[\lambda(p - P_1(\alpha)) + \mu(p - P_2(\alpha)) + \eta \cdot (\alpha, p)]} d\lambda d\mu dp d\alpha, \end{aligned}$$

where the integral is understood in the sense of distributions. To compute the Fourier transform, $\tilde{g}_a(\eta)$, we view $g_a(\alpha, p)$ as a function on \mathbb{R}^2 , which is extended by zero outside M_0 . Set $\eta = r\vec{\Theta}$, $\vec{\Theta} = (\Theta_\alpha, \Theta_p) \in S^1$, $r > 0$.

Change the variables $\check{\lambda} = \lambda/r$ and $\check{\mu} = \mu/r$:

$$(7.5) \quad \tilde{g}_a(r\vec{\Theta}) = r^2 \frac{\Gamma^2(3/2)e(-3)}{(2\pi)^2} \int_{M_0} \int_{\mathbb{R}} \int_{\mathbb{R}} (r\check{\lambda} - i0)^{-3/2} (r\check{\mu} - i0)^{-3/2} B(\alpha, p) \\ \times e^{ir[\check{\lambda}(p-P_1(\alpha)) + \check{\mu}(p-P_2(\alpha)) + \vec{\Theta} \cdot (\alpha, p)]} d\check{\lambda} d\check{\mu} dp d\alpha.$$

The stationary point of the phase is determined by solving the following system:

$$(7.6) \quad \begin{aligned} p - P_1(\alpha) &= 0, \quad p - P_2(\alpha) = 0, \\ -\check{\lambda}P'_1(\alpha) - \check{\mu}P'_2(\alpha) + \Theta_\alpha &= 0, \quad \check{\lambda} + \check{\mu} + \Theta_p = 0. \end{aligned}$$

As is easily seen, the stationary point $(\alpha, p, \check{\lambda}, \check{\mu})$ is given by

$$(7.7) \quad \alpha_0, p_0, \check{\lambda}_0(\eta) = \frac{\eta \cdot (1, P'_2(\alpha_0))}{P'_1(\alpha_0) - P'_2(\alpha_0)}, \check{\mu}_0(\eta) = \frac{\eta \cdot (1, P'_1(\alpha_0))}{P'_2(\alpha_0) - P'_1(\alpha_0)}, \eta = \vec{\Theta}.$$

The Hessian matrix is given by

$$(7.8) \quad H = \begin{pmatrix} 0 & V \\ V^\top & W \end{pmatrix}, \quad V = \begin{pmatrix} -P'_1(\alpha_0) & 1 \\ -P'_2(\alpha_0) & 1 \end{pmatrix}, \quad W = \begin{pmatrix} -\check{\lambda}P''_1(\alpha_0) - \check{\mu}P''_2(\alpha_0) & 0 \\ 0 & 0 \end{pmatrix}.$$

The determinant of the Hessian at the stationary point is $(P'_1(\alpha_0) - P'_2(\alpha_0))^2 \neq 0$. Using Sylvester's law of inertia, it is not hard to show that the number of positive and negative eigenvalues of H are the same. By the stationary point method,

$$(7.9) \quad \begin{aligned} \tilde{g}_a(r\vec{\Theta}) &= C \frac{Q(\vec{\Theta})}{r^3} e^{ir\vec{\Theta} \cdot (\alpha_0, p_0)} + O(r^{-4}), \quad r \rightarrow +\infty, \\ Q(\eta) &:= e(-3)(\check{\lambda}_0(\eta) - i0)^{-3/2}(\check{\mu}_0(\eta) - i0)^{-3/2} = \kappa |\check{\lambda}_0(\eta)\check{\mu}_0(\eta)|^{-3/2}, \\ C &:= \frac{\Gamma^2(3/2)B(\alpha_0, p_0)}{|P'_1(\alpha_0) - P'_2(\alpha_0)|}, \quad \kappa = e(-(3/2)[\text{sgn}(\check{\lambda}_0(\eta)) + \text{sgn}(\check{\mu}_0(\eta))]. \end{aligned}$$

It is easy to verify that $Q(-\eta) = \overline{Q}(\eta)$, where the bar denotes the complex conjugation. Also, $\check{\lambda}_0(\eta) \neq 0$ and $\check{\mu}_0(\eta) \neq 0$ if

$$(7.10) \quad \eta \cdot (1, P'_j(\alpha_0)) \neq 0, \quad j = 1, 2.$$

This assumption is made in what follows. By considering different values of $\text{sgn}(\lambda_0)$ and $\text{sgn}(\mu_0)$, we compute the corresponding values of κ using (7.9), see Table 1.

$\text{sgn}(\lambda_0)$	$\text{sgn}(\mu_0)$	κ
+	+	i
+	-	1
-	+	1
-	-	$-i$

TABLE 1. The signs of $\check{\lambda}_0$ and $\check{\mu}_0$ and the corresponding values of κ .

In a slightly different form, (7.9) is

$$(7.11) \quad \tilde{g}_a(\eta) = Ce^{i\eta \cdot (\alpha_0, p_0)} Q(\eta) + O(|\eta|^{-4}), \quad |\eta| \rightarrow \infty.$$

We select a function $\chi \in C_0^\infty(\mathbb{R}^2)$ supported in a sufficiently small neighborhood of $(\alpha_0, -\vec{\alpha}_0^\perp \cdot x_0)$, which equals 1 in a smaller neighborhood of that point.

The reconstruction can be written as follows

$$(7.12) \quad \begin{aligned} f_a(x) &\doteq \frac{1}{(2\pi)^3} \int_{\mathbb{R}} \int_{\mathbb{R}^2} \chi(\alpha, \eta_\alpha/\eta_p) |\eta_p| \tilde{g}_a(\eta) e^{-i\eta \cdot (\alpha, \vec{\alpha} \cdot x)} d\eta d\alpha \\ &\doteq \frac{C}{(2\pi)^3} \int_{\mathbb{R}} \int_{\mathbb{R}} \int_{\mathbb{R}} \chi(\alpha, \eta_\alpha/\eta_p) |\eta_p| [Q(\eta) + O(|\eta|^{-4})] \\ &\quad \times e^{-i\eta \cdot (\alpha - \alpha_0, \vec{\alpha} \cdot x - p_0)} d\eta_\alpha d\alpha d\eta_p, \end{aligned}$$

where the above integrals are understood as oscillatory. Here, \doteq denotes equality up to a function, which is C^∞ in a small neighborhood of x_0 . This follows from (2.8), (2.10), and assumption $\text{supp}(g_a) \subset M_0$. Since $x_0 \neq x_{1,2}$, it follows that (7.10) is satisfied whenever $\chi(\alpha, \eta_\alpha/\eta_p) \neq 0$.

Suppose $\eta_p > 0$. Consider the double integral with respect to η_α and α . Changing variables $\eta_\alpha \rightarrow \check{\eta}_\alpha = \eta_\alpha/\eta_p$ we get

$$(7.13) \quad I_+(\eta_p) = \eta_p^{-1} \int_{\mathbb{R}^2} \chi(\alpha, \check{\eta}_\alpha) [Q(\check{\eta}_\alpha, 1) + O(\eta_p^{-1})] e^{-i\eta_p(\check{\eta}_\alpha, 1) \cdot (\alpha - \alpha_0, \vec{\alpha} \cdot x - p_0)} d\check{\eta}_\alpha d\alpha,$$

where the big- O term is understood as $\eta_p \rightarrow +\infty$. Since χ is compactly supported, the double integral is over a bounded set. The stationary point is

$$(7.14) \quad \alpha = \alpha_0, \quad \check{\eta}_\alpha = -\vec{\alpha}_0^\perp \cdot x.$$

By the stationary phase method,

$$(7.15) \quad I_+(\eta_p) = 2\pi Q(-\vec{\alpha}_0^\perp \cdot x, 1) \eta_p^{-2} e^{-i\eta_p(\vec{\alpha}_0 \cdot x - p_0)} + O(\eta_p^{-3}), \quad \eta_p \rightarrow +\infty.$$

Suppose next $\eta_p < 0$. Consider the double integral with respect to η_α and α . Changing variables $\eta_\alpha \rightarrow \check{\eta}_\alpha = -\eta_\alpha/\eta_p$ we get

$$(7.16) \quad \begin{aligned} I_-(\eta_p) &= |\eta_p|^{-1} \int_{\mathbb{R}} \int_{\mathbb{R}} \chi(\alpha, -\check{\eta}_\alpha) [Q(\check{\eta}_\alpha, -1) + O(|\eta_p|^{-1})] \\ &\quad \times e^{i(-\eta_p)(-\check{\eta}_\alpha, 1) \cdot (\alpha - \alpha_0, \vec{\alpha} \cdot x - p_0)} d\check{\eta}_\alpha d\alpha. \end{aligned}$$

The stationary point is

$$(7.17) \quad \alpha = \alpha_0, \quad \check{\eta}_\alpha = \vec{\alpha}_0^\perp \cdot x.$$

By the stationary phase method,

$$(7.18) \quad I_-(\eta_p) = 2\pi Q(\vec{\alpha}_0^\perp \cdot x, -1) \eta_p^{-2} e^{-i\eta_p(\vec{\alpha}_0 \cdot x - p_0)} + O(|\eta_p|^{-3}), \quad \eta_p \rightarrow -\infty.$$

Denote

$$(7.19) \quad Q_0 = Q(-\vec{\alpha}_0^\perp \cdot x_0, 1).$$

By (7.7),

$$(7.20) \quad \begin{aligned} \check{\lambda}_0(-\vec{\alpha}_0^\perp \cdot x_0, 1) &= \frac{P'_2(\alpha_0) - \vec{\alpha}_0^\perp \cdot x_0}{P'_1(\alpha_0) - P'_2(\alpha_0)}, \\ \check{\mu}_0(-\vec{\alpha}_0^\perp \cdot x_0, 1) &= \frac{P'_1(\alpha_0) - \vec{\alpha}_0^\perp \cdot x_0}{P'_2(\alpha_0) - P'_1(\alpha_0)}. \end{aligned}$$

By (7.12), (7.15), and (7.18),

$$(7.21) \quad f_a(x_0 + h\vec{\alpha}_0) \sim \frac{C}{(2\pi)^2} \left[Q_0 \int_0^\infty \eta_p^{-2} e^{-i\eta_p h} d\eta_p + \overline{Q}_0 \int_{-\infty}^0 \eta_p^{-2} e^{-i\eta_p h} d\eta_p \right],$$

where \sim denotes equality up to a $I^{-3}(N^*0)$ function. Using entries 20 and 28 in the Table of Fourier Transforms of [11], the expression in brackets can be written as follows

$$(7.22) \quad \begin{aligned} &(\operatorname{Re} Q_0) \mathcal{F}(\eta_p^{-2})(-h) + i(\operatorname{Im} Q_0) \mathcal{F}(\eta_p^{-2} \operatorname{sgn} \eta_p)(-h) \\ &\sim (\operatorname{Re} Q_0) |h| + (\operatorname{Im} Q_0) 2h \ln |h|. \end{aligned}$$

Therefore the leading singularity of f_a is given by

$$(7.23) \quad \begin{aligned} f_a(x_0 + h\vec{\alpha}_0) &\sim C_0 [(\operatorname{Re} \kappa) |h| + (\operatorname{Im} \kappa) 2h \ln |h|], \\ C_0 &:= \frac{B(\alpha_0, p_0)}{16\pi} \frac{|P'_1(\alpha_0) - P'_2(\alpha_0)|^2}{|(\vec{\alpha}_0^\perp \cdot x_0 - P'_1(\alpha_0))(\vec{\alpha}_0^\perp \cdot x_0 - P'_2(\alpha_0))|^{3/2}}, \end{aligned}$$

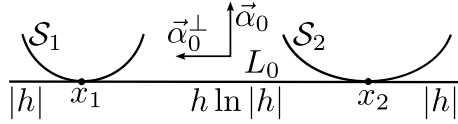


FIGURE 6. The case where local segments \mathcal{S}_1 (near x_1) and \mathcal{S}_2 (near x_2) of \mathcal{S} are on one side of the double tangent L_{p_0} .

7.2. Example. To illustrate (7.23), consider the following example. Recall that x_1 and x_2 are the points at which L_{p_0} is tangent to \mathcal{S} (see Figure 6). Suppose that $\vec{\alpha}_0$ points to the half-plane containing the centers of curvature of \mathcal{S} at x_1 and x_2 . Finally, suppose, $\vec{\alpha}_0^\perp = (x_1 - x_2)/|x_1 - x_2|$. We draw $\vec{\alpha}_0$ pointing up and $\vec{\alpha}_0^\perp$ pointing to the left. Thus, x_1 is to the left of x_2 and $\vec{\alpha}_0^\perp \cdot x_2 < \vec{\alpha}_0^\perp \cdot x_1$.

As can be easily seen, $P'_2(\alpha_0) < P'_1(\alpha_0)$. This holds because $P'_j(\alpha_0) = \vec{\alpha}_0^\perp \cdot x_j$, $j = 1, 2$. The last statement is used in case 3 of section 6 as the basis for the claim that Γ_j is tangent to Γ_{x_0} and \mathbf{p}_j , $j = 1, 2$, see Figure 3. Another variation on the same theme is in case 5 of section 6, see Figure 5. Furthermore,

$$(7.24) \quad \begin{aligned} &P'_2(\alpha_0) < P'_1(\alpha_0) < \vec{\alpha}_0^\perp \cdot x_0 \text{ if } x_0 \in (-\infty, x_1), \\ &P'_2(\alpha_0) < \vec{\alpha}_0^\perp \cdot x_0 < P'_1(\alpha_0) \text{ if } x_0 \in (x_1, x_2), \\ &\vec{\alpha}_0^\perp \cdot x_0 < P'_2(\alpha_0) < P'_1(\alpha_0) \text{ if } x_0 \in (x_2, \infty). \end{aligned}$$

By (7.20),

$$(7.25) \quad \begin{aligned} \operatorname{sgn}(\lambda_0) &= -1, \operatorname{sgn}(\mu_0) = +1 \text{ if } x_0 \in (-\infty, x_1), \\ \operatorname{sgn}(\lambda_0) &= -1, \operatorname{sgn}(\mu_0) = -1 \text{ if } x_0 \in (x_1, x_2), \\ \operatorname{sgn}(\lambda_0) &= +1, \operatorname{sgn}(\mu_0) = -1 \text{ if } x_0 \in (x_2, \infty). \end{aligned}$$

From Table 1, the values of κ for all $x_0 \in L_{\mathbf{p}_0} \setminus \{x_1, x_2\}$ are given by

$$(7.26) \quad \kappa = \begin{cases} -i, & x_0 \in (x_1, x_2), \\ 1, & x_0 \in L_{\mathbf{p}_0} \setminus [x_1, x_2]. \end{cases}$$

Together with (7.23) this implies, up to a positive factor, (see (4.16) and Figure 6)

$$(7.27) \quad f_a(x_0 + h\vec{\alpha}_0) \sim B_{\frac{1}{2}, \frac{1}{2}}(\mathbf{p}_0) \begin{cases} h \ln |h|, & x_0 \in (x_1, x_2), \\ |h|, & x_0 \in L_{\mathbf{p}_0} \setminus [x_1, x_2]. \end{cases}$$

For illustration purposes, the graph of the function $h \log |h|$, $|h| \leq 0.5$, is shown in Figure 7.

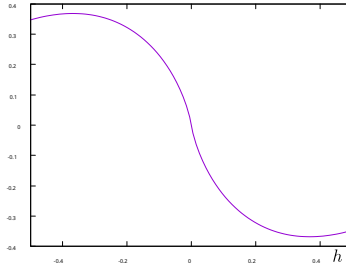


FIGURE 7. Plot of the function $h \log |h|$.

8. $+-$ CASE

Suppose now that

$$(8.1) \quad g_a(\alpha, p) = (p - P_1(\alpha))_-^{1/2} (p - P_2(\alpha))_+^{1/2} B(\alpha, p), \quad B \in C_0^\infty(M_0).$$

Using (7.3) and entry 25 in the Table of Fourier Transforms of [11]

$$(8.2) \quad p_-^{1/2} = \frac{\Gamma(3/2)e(3/2)}{2\pi} \int_{\mathbb{R}} (\lambda + i0)^{-3/2} e^{i\lambda p} d\lambda,$$

we obtain analogously to (7.9) and (7.11), assuming (7.10) holds:

$$(8.3) \quad \begin{aligned} \tilde{g}_a(\eta) &= CQ(\eta)e^{i\eta \cdot (\alpha_0, p_0)} + O(|\eta|^{-4}), \quad |\eta| \rightarrow +\infty, \\ Q(\eta) &:= (\check{\lambda}_0(\eta) - i0)^{-3/2} (\check{\mu}_0(\eta) + i0)^{-3/2} = \kappa |\check{\lambda}_0(\eta)\check{\mu}_0(\eta)|^{-3/2}, \\ \kappa &:= e((3/2)[- \operatorname{sgn}(\check{\lambda}_0(\eta)) + \operatorname{sgn}(\check{\mu}_0(\eta))]), \end{aligned}$$

where $\check{\lambda}_0(\eta)$ and $\check{\mu}_0(\eta)$ are the same as in (7.7), and C is the same as in (7.9). As before, $Q(-\eta) = \overline{Q}(\eta)$. Therefore, (7.11)–(7.23) still apply, but with the new definition of Q .

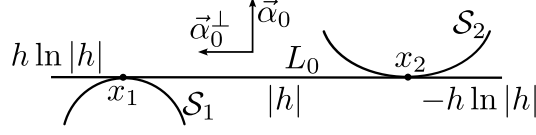


FIGURE 8. The case where local segments \mathcal{S}_1 (near x_1) and \mathcal{S}_2 (near x_2) of \mathcal{S} are on opposite sides of the double tangent L_{p_0} .

To illustrate this case, we choose $\vec{\alpha}_0$ and $\vec{\alpha}_0^\perp$ in the same way as before, but \mathcal{S}_1 is now below L_{p_0} (see Figure 8). As is easily seen, (7.24) and (7.25) still hold. Substituting (7.25) into the definition of κ in (8.3) we find

$$(8.4) \quad \kappa = \begin{cases} -i, & x_0 \in (-\infty, x_1), \\ 1, & x_0 \in (x_1, x_2), \\ i, & x_0 \in (x_2, \infty). \end{cases}$$

Together with (7.23) this implies that up to a positive factor one has (see Figure 8)

$$(8.5) \quad f_a(x_0 + h\vec{\alpha}_0) \sim B_{\frac{1}{2}, \frac{1}{2}}(p_0) \begin{cases} h \ln |h|, & x_0 \in (-\infty, x_1), \\ |h|, & x_0 \in (x_1, x_2), \\ -h \ln |h|, & x_0 \in (x_2, \infty). \end{cases}$$

9. NUMERICAL EXPERIMENTS

We use a two-ball phantom for the numerical experiments. The two balls have the following centers, c_k , and radii, R_k :

$$(9.1) \quad c_1 = (-1.8, -2), \quad R_1 = 1.8, \quad c_2 = (2.1, 2.2), \quad R_2 = 1.7.$$

The two basis functions, μ_1 , μ_2 , and the normalized product of the X-ray beam energy spectrum and detector efficiency, $\rho(E)$, are given by (see Figure 9)

$$(9.2) \quad \begin{aligned} \mu_1(E) &= 4.1 \exp(-2.5E), \quad \mu_2(E) = 3 \exp(-0.5E), \\ \rho(E) &= \frac{35}{16} (1 - (2E - 1)^2)^3, \quad 0 \leq E \leq E_{\text{mx}} = 1. \end{aligned}$$

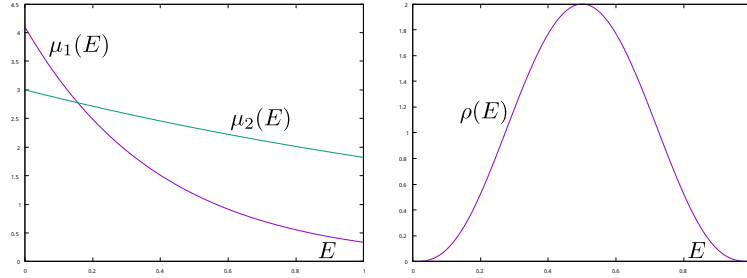


FIGURE 9. Basis functions $\mu_1(E)$ and $\mu_2(E)$ and the energy spectrum $\rho(E)$.

Data $G(\alpha, p)$ are computed using (1.7), where f_k is the characteristic function of the k -th ball. We use

$$(9.3) \quad \begin{aligned} N_\alpha &= 10^4, \quad \Delta_\alpha = \pi/N_\alpha, \quad N_p = 15001, \quad \Delta_p = 2R_{\text{FOV}}/(N_p - 1), \\ \alpha_k &= \Delta_\alpha k, \quad 0 \leq k < N_\alpha, \quad p_j = -R_{\text{FOV}} + \Delta_p j, \quad 0 \leq j < N_p. \end{aligned}$$

Here R_{FOV} is the radius of the field of view (FOV).

The reconstruction is computed using (7.2). We denote the reconstructed function f^{rec} instead of f_a as in (7.2), because in computations we use the complete function $g(\mathbf{p})$ rather than its paired Lagrangian part g_a . The ramp kernel is smoothed by convolving it with a small radius mollifier

$$(9.4) \quad w(t) = \frac{15}{16\epsilon} (1 - (t/\epsilon)^2)^2, \quad \epsilon = 0.015,$$

to avoid aliasing.

Global plots of $f^{\text{rec}}(x)$ are shown in Figure 10 and Figure 11. Figure 10 shows $f^{\text{rec}}(x)$ in the full grayscale window. The right panel in the figure clearly demonstrates low-frequency cupping artifacts, which are caused by beam hardening. The plot on the right is along the yellow line on the left. Figure 11 shows $f^{\text{rec}}(x)$ in the narrow grayscale window $[-0.12, 0.06]$. In other words, for display purposes, if $f^{\text{rec}}(x) > 0.06$ at some x , we set $f^{\text{rec}}(x) = 0.06$. Similarly, if $f^{\text{rec}}(x) < -0.12$ at some x , we set $f^{\text{rec}}(x) = -0.12$. This window is selected to better illustrate the high-frequency BHA.

Reconstructions are also computed on a dense grid in a neighborhood of several points x_0 on the double tangent lines L_1, L_2 , see Figure 12. Points x_0 on these lines are parameterized by $\nu \in \mathbb{R}$ as follows:

$$(9.5) \quad x_0 = x_1 + \nu(x_2 - x_1) \in L_1, \quad \nu \neq 0, 1,$$

and similarly for $x_0 \in L_2$ using x_3, x_4 in place of x_1, x_2 . To help visualize what our predictions imply for the two-disk phantom we combine Figure 6 and Figure 8 into a single Figure 12.

The results of the reconstructions in the $++$ case are shown in Figure 13. The three plots represent the graphs of $f^{\text{rec}}(x)$ across three short-line segments perpendicular to L_1 and crossing L_1 at three locations corresponding to $\nu = -0.4, 0.4, 1.3$. The line segments are parameterized as $x = x_0 + h\vec{\alpha}_1$, $|h| \leq 0.25$. Qualitatively, the behavior of f^{rec} matches our prediction in (7.27), cf. Figure 12. The left and right graphs in Figure 13 are shaped like $|h|$, and the middle graph is shaped like $h \ln |h|$ (cf. Figure 7). Note that the $|h|$ -shaped graphs in the left and right panels point in the same direction, which also agrees with (7.27).

In this and the next case, the $|h|$ -shaped curves look like a rotated graph of the function $y = |x|$ because of the contribution of smooth terms to f^{rec} that are ignored by our analysis.

The results of the reconstructions in the $+ -$ case are shown in Figure 14. The three plots represent the graphs of $f^{\text{rec}}(x)$ across three short-line segments perpendicular to L_2 and crossing L_2 at three locations corresponding to $\nu = -0.4, 0.4, 1.3$. The line segments are parameterized as $x = x_0 + h\vec{\alpha}_2$, $|h| \leq 0.25$. Qualitatively, the behavior of f^{rec} matches our prediction in (8.5), cf. Figure 12. The left and right graphs in Figure 14 are shaped like $h \ln |h|$, and the middle graph is shaped like $|h|$. Note that the $h \ln |h|$ -shaped

graphs in the left and right panels have prefactors of opposite signs, which is also in agreement with (8.5).

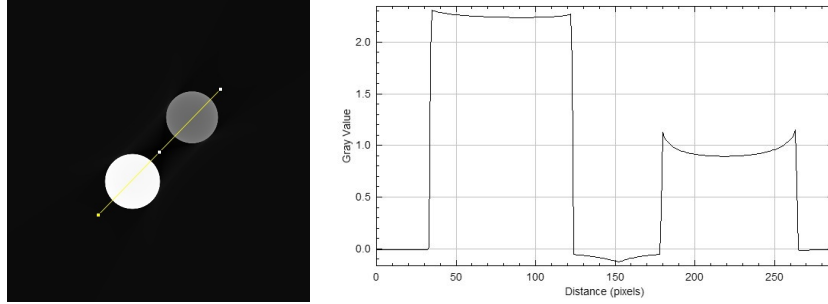


FIGURE 10. Global reconstruction, wide display window. Typical cupping caused by beam hardening is clearly visible. The plot on the right is along the yellow line shown on the left.

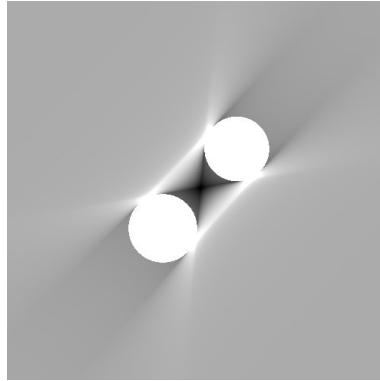


FIGURE 11. Global reconstruction, narrow display window to better see artifacts. $WL=-0.03$, $WW=0.18$.

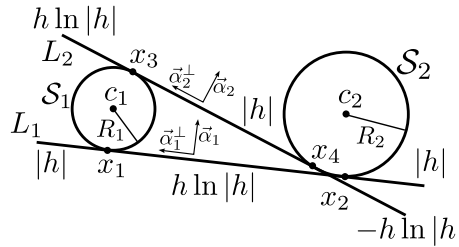


FIGURE 12. Illustration of the two-ball phantom used in the numerical experiment. The line L_1 corresponds to the $++$ case (section 7), and the line L_2 - to the $+-$ case (section 8).

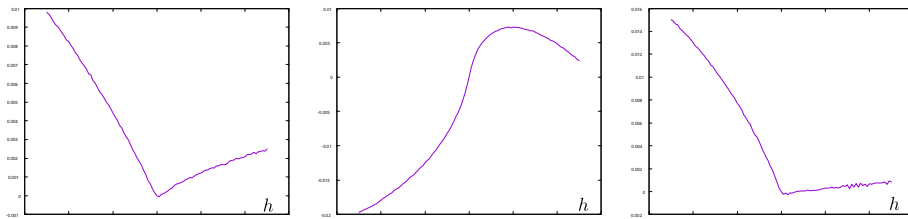


FIGURE 13. Profiles through the artifact at three points on L_1 , ++ case. Left: $x_0 \in (-\infty, x_1)$, $\nu = -0.4$; middle: $x_0 \in (x_1, x_2)$, $\nu = 0.4$; right: $x_0 \in (x_2, \infty)$, $\nu = 1.3$.

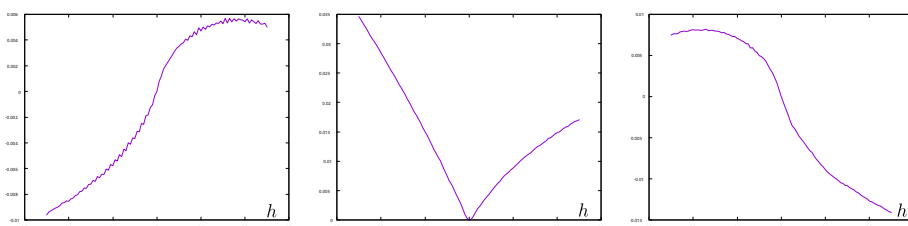


FIGURE 14. Profiles through the artifact at three points on L_2 , +- case. Left: $x_0 \in (-\infty, x_3)$, $\nu = -0.4$; middle: $x_0 \in (x_3, x_4)$, $\nu = 0.4$; right: $x_0 \in (x_4, \infty)$, $\nu = 1.3$.

REFERENCES

- [1] R. G. Airapetyan and A. G. Ramm. Singularities of the Radon transform. *Applicable Analysis*, 79(3-4):351–379, 2001.
- [2] A. M. Alessio and L. R. MacDonald. Quantitative material characterization from multi-energy photon counting CT. *Medical Physics*, 40(3):1–8, 2013.
- [3] R. E. Alvarez. Estimator for photon counting energy selective x-ray imaging with multibin pulse height analysis. *Medical Physics*, 38(5):2324–2334, 2011.
- [4] R. E. Alvarez and A. Macovski. Energy-selective reconstructions in X-ray computerised tomography. *Physics in Medicine and Biology*, 21(5):733–744, 1976.
- [5] G. Bal and F. Terzioglu. Uniqueness criteria in multi-energy CT. *Inverse Problems*, 36(6), 2020.
- [6] H. Chihara. Microlocal analysis of d -plane transform on the Euclidean space. *SIAM Journal of Mathematical Analysis*, 54(6):6254–6287, 2022.
- [7] W. Dewulf, Y. Tan, and K. Kiekens. Sense and non-sense of beam hardening correction in CT metrology. *CIRP Annals - Manufacturing Technology*, 61(1):495–498, 2012.
- [8] R. S. Ellis. *Entropy, Large Deviations, and Statistical Mechanics*. Springer-Verlag, New York, 1985.
- [9] C. L. Epstein. *Introduction to the Mathematics of Medical Imaging*. SIAM, Philadelphia, second edition, 2008.
- [10] R. Forghani, B. De Man, and R. Gupta. Dual-Energy Computed Tomography: Physical Principles, Approaches to Scanning, Usage, and Implementation: Part 1. *Neuroimaging Clinics of North America*, 27(3):371–384, 2017.
- [11] I. M. Gel’fand and G. E. Shilov. *Generalized Functions, Volume I. Properties and Operations*. AMS Chelsea Publishing, Providence, RI, reprinted edition, 1964.
- [12] V. Guillemin and G. Uhlmann. Oscillatory integrals with singular symbols. *Duke Mathematical Journal*, 48(1):251–267, 1981.
- [13] L. Hormander. *The Analysis of Linear Partial Differential Operators III. Pseudo-Differential Operators*. Springer-Verlag, Berlin, 1994.

- [14] L. Hormander. *The Analysis of Linear Partial Differential Operators IV. Fourier Integral Operators*. Springer-Verlag, Berlin, 2009.
- [15] P. M. Joseph and R. D. Spital. A method for correcting bone induced artifacts in computed tomography scanners. *Journal of Computer Assisted Tomography*, 2(1):100–108, 1978.
- [16] Y. Kyriakou, E. Meyer, D. Prell, and M. Kachelrieß. Empirical beam hardening correction (EBHC) for CT. *Medical Physics*, 37(10):5179–5187, 2010.
- [17] C. H. McCollough, K. Boedeker, D. Cody, X. Duan, T. Flohr, S. S. Halliburton, J. Hsieh, R. R. Layman, and N. J. Pelc. Principles and applications of multienergy CT: Report of AAPM Task Group 291. *Medical Physics*, 47(7):e881–e912, 2020.
- [18] R. B. Melrose and G. A. Uhlmann. Lagrangian Intersection and the Cauchy Problem. *Communications on Pure and Applied Mathematics*, 32(4):483–519, 1979.
- [19] B. Palacios, G. Uhlmann, and Y. Wang. Quantitative analysis of metal artifacts in X-ray tomography. *SIAM Journal on Mathematical Analysis*, 50(5):4914–4936, 2018.
- [20] V. P. Palamodov. Nonlinear artifacts in tomography. *Soviet Physics Doklady*, 31(11):888–890, 1986.
- [21] V. P. Palamodov. Some singular problems in tomography. *Translations of mathematical monographs*, 81:123–140, 1990.
- [22] H. S. Park, J. K. Choi, and J. K. Seo. Characterization of Metal Artifacts in X-Ray Computed Tomography. *Communications on Pure and Applied Mathematics*, 70(11):2191–2217, 2017.
- [23] M. Paziresh, A. M. Kingston, S. J. Latham, W. K. Fullagar, and G. M. Myers. Tomography of atomic number and density of materials using dual-energy imaging and the Alvarez and Macovski attenuation model. *Journal of Applied Physics*, 119(21), 2016.
- [24] E. B. Podgorsak. *Radiation Physics for Medical Physicists*. Springer-Verlag, Berlin, Heidelberg, 2nd edition, 2010.
- [25] A. G. Ramm and A. I. Zaslavsky. Singularities of the Radon transform. *Bulletin of the American Mathematical Society*, 28(1):109–115, 1993.
- [26] A. G. Ramm and A. I. Zaslavsky. X-Ray Transform, the Legendre Transform, and Envelopes. *Journal of Mathematical Analysis and Applications*, 183(3):528–546, 1994.
- [27] E. Roessl and R. Proksa. K-edge imaging in x-ray computed tomography using multi-bin photon counting detectors. *Physics in Medicine and Biology*, 52(15):4679–4696, 2007.
- [28] D. Sanderson, C. Martinez, J. A. Fessler, M. Desco, and M. Abella. Statistical image reconstruction with beam-hardening compensation for X-ray CT by a calibration step (2DIterBH). In *Medical Physics*, volume 51, pages 5204–5213, 2024.
- [29] S. Schüller, S. Sawall, K. Stannigel, M. Hülsbusch, J. Ulrici, E. Hell, and M. Kachelrieß. Segmentation-free empirical beam hardening correction for CT. *Medical Physics*, 42(2):794–803, 2015.
- [30] T. Sellerer, S. Ehn, K. Mechlem, M. Duda, M. Eppe, P. B. Noël, and F. Pfeiffer. Quantitative dual-energy micro-CT with a photon-counting detector for material science and non-destructive testing. *PLoS ONE*, 14(7):1–18, 2019.
- [31] X. Wang, D. Meier, K. Taguchi, D. J. Wagenaar, B. E. Patt, and E. C. Frey. Material separation in x-ray CT with energy resolved photon-counting detectors. *Medical Physics*, 38(3):1534–1546, 2011.
- [32] Y. Wang. Identification of nonlinear beam-hardening effects in X-ray tomography. *SIAM Journal of Mathematical Analysis*, 56(6):7290–7305, 2023.
- [33] Y. Wang and Y. Zou. Streak Artifacts From Nonconvex Metal Objects in X-Ray Tomography. *Pure and Applied Analysis*, 3(2):295–318, 2021.